Journal of Applied Physics

RESEARCH ARTICLE | NOVEMBER 16 2022

Polarization-selective magneto-optical modulation

Banoj Kumar Nayak ; Eyal Buks

J. Appl. Phys. 132, 193905 (2022)
https://doi.org/10.1063/5.0128647

Journal of Applied Physics ARTICLE scitation.org/journal/jap

Polarization-selective magneto-optical modulation

Cite as: J. Appl. Phys. **132**, 193905 (2022); doi: 10.1063/5.0128647
Submitted: 29 September 2022 · Accepted: 26 October 2022 ·
Published Online: 16 November 2022

Banoj Kumar Nayak and Eyal Buks[a)]

AFFILIATIONS

Andrew and Erna Viterbi Department of Electrical Engineering, Technion, Haifa 32000, Israel

[a)]**Author to whom correspondence should be addressed:** eyal@technion.ac.il

ABSTRACT

We study magneto-optical coupling in a ferrimagnetic sphere resonator made of yttrium iron garnet. We find that the resonator can be operated in the telecom band as a polarization-selective optical modulator. The input state of polarization (SOP) contributing to the Stokes sideband is orthogonal to the one contributing to the anti-Stokes sideband. In the region of single sideband modulation, the SOP of both sidebands is nearly orthogonal to the SOP of the incident light. Intermodulation gain can be employed in the nonlinear regime for amplification.

I. INTRODUCTION

Information is commonly transmitted by modulating a monochromatic carrier wave. The method of single sideband modulation (SSM) allows reducing both transmission power and bandwidth, in comparison with simpler methods such as amplitude, frequency, and phase modulation.[1] In the radio frequency band, SSM can be implemented using electronic circuits, however, SSM implementation in the optical band is challenging, since it requires that different out of phase modulation methods are simultaneously applied.[2,3]

Magneto-optical (MO) coupling[4–10] in ferrimagnetic sphere resonators (FSRs) can be used for optical modulation of signals in the microwave band. Such a modulation has been demonstrated before[11–21] by exciting individual whispering gallery FSR optical modes using either a tapered optical fiber or a prism. Here, we employed a modified experimental setup, in which light in the telecom band is transmitted through the FSR bulk. Driving the FSR near its resonance generates sidebands in the transmitted optical spectrum. We find that the FSR can be used as a polarization-selective SSM. The polarization selectivity is attributed to angular momentum conservation in photon-magnon scattering.[22–27] We demonstrate that intermodulation gain can be exploited in the nonlinear regime for amplification.

II. EXPERIMENTAL SETUP

The experimental setup is schematically shown in Fig. 1. Optical components and fibers are red colored, whereas blue color is used to label microwave (MW) components and coaxial cables. A MW cavity made of a loop gap resonator (LGR) allows achieving a relatively large coupling between magnons and MW photons.[29–32] The LGR is fabricated from a hollow concentric aluminum tube. A sapphire (S) strip of 260 μm thickness is inserted into the gap in order to increase its capacitance, which in turn reduces the frequency f_c of the LGR fundamental mode. An FSR made of yttrium iron garnet (YIG) having a radius of $R_s = 125\,\mu\text{m}$ is held by two ceramic ferrules (CFs) inside the LGR. The two CFs, which are held by a concentric sleeve, provide transverse alignment for both input and output single mode optical fibers. Fiber vertical alignment is performed by maximizing optical transmission.

The angular frequency of the Kittel mode ω_m is approximately given by $\omega_m = \mu_0 \gamma_e H_s$, where H_s is the static magnetic field, μ_0 is the free space permeability, and $\gamma_e/2\pi = 28\,\text{GHz}\,\text{T}^{-1}$ is the gyromagnetic ratio.[10] The applied static magnetic field $\mathbf{H}_s$ is controlled by adjusting the relative position of a magnetized neodymium using a motorized stage. The static magnetic field is normal to the light propagation direction $\mathbf{k}$, and the magnetic field of MW drive is nearly parallel to $\mathbf{k}$. The LGR-FSR coupled system is encapsulated inside a metallic rectangular shield made of aluminum. The LGR is weakly coupled to a microwave loop antenna (MWA).

The plot in Fig. 2 exhibits a vector network analyzer (VNA) reflectivity measurement of the LGR-FSR coupled system. The static applied magnetic field H_s in this measurement is varied near the value corresponding to avoided-crossing between the FSR and LGR resonances.

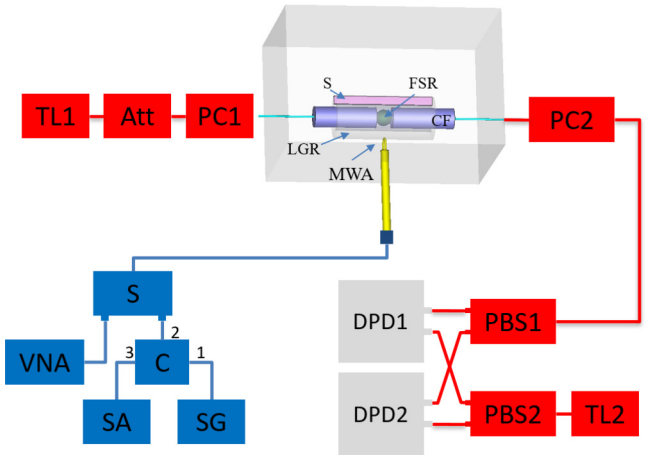

FIG. 1. Experimental setup. Optical fibers are installed on both sides of the FSR for transmission of light through the sphere. Optical components [TL (tunable laser), Att (optical attenuator), PC (polarization controller), and PBS (polarization beam splitter)] and fibers are red colored, and MW components [MWA (microwave loop antenna), S (splitter), C (circulator), VNA (vector network analyzer), SA (spectrum analyzer), and SG (signal generator)] and coaxial cables are blue colored. TL2 together with two PBSs (labeled as PBS1 and PBS2) and two differential photodetectors (labeled as DPD1 and DPD2) operate as a polarization-selective optical spectrum analyzer.[28] A power amplifier is serially connected to the SG. The MWA is weakly coupled to the FSR-LGR system.

III. OPTICAL SIDEBANDS

Optical sidebands are observed in the transmission spectrum when the driving microwave frequency $\omega_p/(2\pi)$ is tuned close to the FSR resonance at $\omega_m/(2\pi)$. The plot shown in Fig. 3 exhibits the measured total optical intensity $I_T = I_{DPD1} + I_{DPD2}$ as a function of the wavelength λ_2 of TL2, where I_{DPD1} and I_{DPD2} are the intensities measured by the two differential photodetectors (labeled as DPD1 and DPD2 in Fig. 1). The sideband wavelengths are given by $\lambda_L \pm \lambda_{SB}$, where $\lambda_{SB} \simeq \lambda_L^2 \omega_p/(2\pi c)$, and λ_L is the TL1 wavelength, which is related to the TL1 frequency $\omega_L/(2\pi)$ by $\omega_L = 2\pi c/\lambda_L$, where c is the speed of light in vacuum. The value of $\lambda_{SB} = 30.0$ pm is obtained for TL1 wavelength of $\lambda_L = 1539$ nm and FSR driving frequency of $\omega_p/(2\pi) = 3.79$ GHz.

Both motorized polarization controllers (labeled as PC1 and PC2 in Fig. 1) have three optomechanical components (paddles), which act as either quarter or half wave plates. The paddles' angles of PC1 (PC2) are denoted by θ_{1A}, θ_{1B}, and θ_{1C} (θ_{2A}, θ_{2B}, and θ_{2C}). The incident light state of polarization (SOP) can be manipulated using PC1. We observe that the intensity of lower wavelength $\lambda_L - \lambda_{SB}$ anti-Stokes sideband and higher wavelength $\lambda_L + \lambda_{SB}$ Stokes sideband depends on the input SOP. SSM in the transmission spectrum, with either single anti-Stokes sideband or single Stokes sideband, can be obtained by adjusting PC1. The plot shown in Fig. 4(a) exhibits the measured anti-Stokes sideband intensity as a function of microwave driving frequency $f_p = \omega_p/(2\pi)$ and PC1 angle θ_{1C} near the avoided-crossing region. The plot shown in Fig. 4(c) exhibits simultaneously measured Stokes sideband intensity in the same region. We clearly observe appreciable anti-Stokes and Stokes intensity in Figs. 4(a) and 4(c), respectively, when driving frequency $\omega_p/(2\pi)$ becomes close to FSR resonance $\omega_m/(2\pi)$. However, they are asymmetric. For a certain range of PC1 position, SSM is obtained, i.e., only one sideband, either anti-Stokes or Stokes, is observed. Contrary to other experimental setups, in which the FSR is optically coupled by either a tapered optical fiber or a prism, for our setup, for which the measured optical transmission only weakly depends on the input wavelength λ_L, SSM can be obtained in a wide range of λ_L.

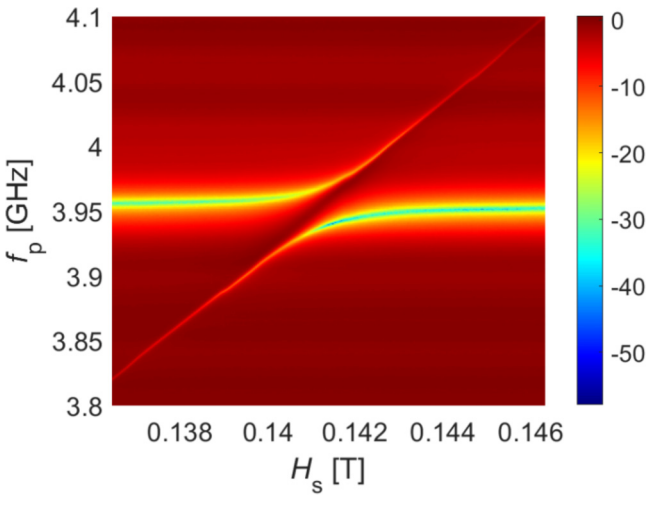

FIG. 2. VNA reflectivity in dB units as a function of magnetic field H_s at an applied microwave power of −30 dBm.

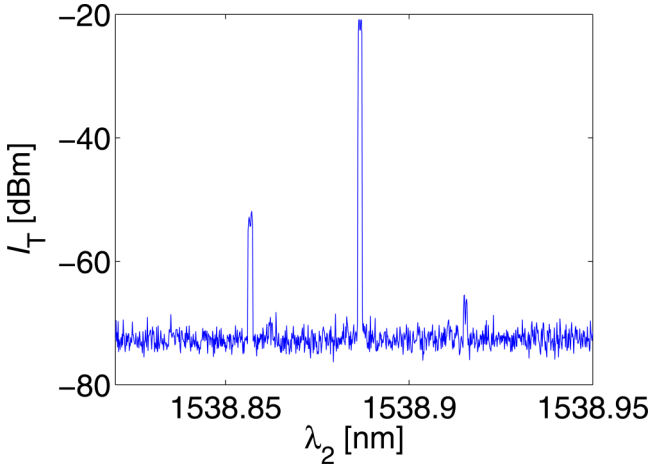

FIG. 3. The transmitted optical spectrum. For this measurement, the TL1 is set at an optical power of 31 mW and a wavelength λ_L of 1538.887 nm, and the driving microwave is set at a frequency $\omega_p/(2\pi)$ of 3.79 GHz and a power of P_p of 20 dBm.

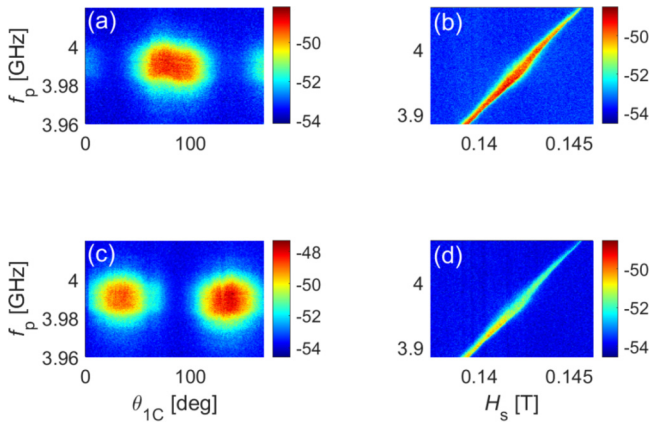

FIG. 4. Sidebands in dBm units. (a) Anti-Stokes intensity as a function of PC1 angle θ_{1C}. (b) Anti-Stokes intensity as a function of magnetic field H_s. (c) Stokes intensity as a function of θ_{1C}. (d) Stokes intensity as a function of H_s. The magnetic field H_s in (a) and (c) is tuned near the avoided-crossing regime. TL1 is set at an optical power of 31 mW and a wavelength of λ_L of 1537.7 nm, and the driving microwave power is set at $P_p = 20$ dBm. In (a) and (c), $\theta_{1A} = 170°$ and $\theta_{1B} = 85°$, and θ_{1C} is varied from 0° to 170°, whereas in (b) and (d) $(\theta_{1A}, \theta_{1B}, \theta_{1C}) = (170°, 85°, 60°)$ (for this setting, both Stokes and anti-Stokes peaks are clearly visible near the FSR resonance).

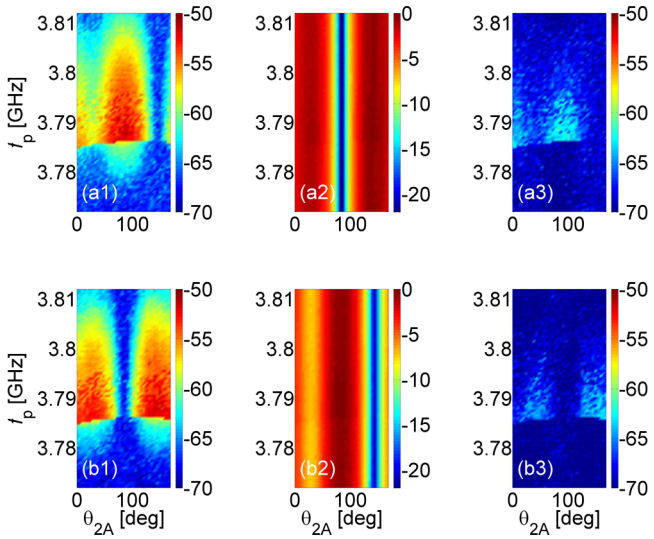

FIG. 5. Sideband SOP. The measured intensity I_{DPD1} (I_{DPD2}) is shown (in dBm units) in the plots labeled by the letter "a" ("b"). The intensity at wavelengths $\lambda_L - \lambda_{SB}$, λ_L and $\lambda_L + \lambda_{SB}$ is shown in the plots labeled by the numbers "1," "2," and "3," respectively. The TL1 is set at an optical power of 31 mW and a wavelength of λ_L of 1538.9 nm, the driving microwave is set at a power P_p of 20 dBm.

A rotating lambda plate polarimeter is employed to measure the input SOP. The polarimeter measurements reveal that the input SOP for the two extreme cases (SSM of either anti-Stokes or Stokes peak) are orthogonal to each other (i.e., separated by a diameter on the Poincaré sphere).

The plots shown in Figs. 4(b) and 4(d) exhibit anti-Stokes and Stokes intensity, respectively, as a function of microwave driving frequency f_p and static magnetic field H_s. The FSR resonance changes as we vary the static magnetic field H_s. Accordingly, from Figs. 4(b) and 4(d), we see that both anti-Stokes and Stokes intensities get pronounced when driving frequency $\omega_p/(2\pi)$ is within the bandwidth of FSR resonance at $\omega_m/(2\pi)$.

Our experimental setup (see Fig. 1) allows measuring the SOP of both sidebands. While the plots shown in Fig. 4 display the total optical intensity $I_T = I_{DPD1} + I_{DPD2}$, the intensity I_{DPD1} (I_{DPD2}) is separately displayed in the top (bottom) row plots shown in Fig. 5. These two intensities I_{DPD1} and I_{DPD2} represent two orthogonal SOP, which can be set by adjusting PC2 (see Fig. 1). The left (right) column plots in Fig. 5 display the measured intensity of the left anti-Stokes (right Stokes) sideband at wavelength $\lambda_L - \lambda_{SB}$ ($\lambda_L + \lambda_{SB}$), whereas the intensity at the central wavelength λ_L is displayed by the central column plots in Fig. 5. For the measurements shown in Fig. 5, PC1 is set to a nearly SSM state. By varying the setting of PC2, we find that the central peak at wavelength λ_L is maximized (minimized) in the same region where the sidebands at wavelength $\lambda_L \pm \lambda_{SB}$ are minimized (maximized). This observation implies that in the region of SSM, the SOP of the sidebands is nearly orthogonal to the SOP of the incident light. This orthogonality can be exploited at the receiver end of a data transmission system based on our proposed MO modulation, since it allows demodulation by polarization filtering-out of the carrier at wavelength λ_L.

IV. MO COUPLING

The MO coupling giving rise to the optical sidebands originates from an interaction term in the system's Hamiltonian, which is denoted by V_{SB}. This term V_{SB} is commonly derived from the classical energy density associated with the interaction between magnetization and optical modes. For the case where only whispering gallery FSR optical modes participate in the interaction, the term V_{SB} was derived in Refs. 11–19, whereas for our experimental configuration we consider the case where light propagates through the FSR bulk.

Consider an incident I (scattered S) optical field, having right and left handed circular polarization amplitudes E_{I+} and E_{I-} (E_{S+} and E_{S-}), respectively. The time-averaged energy density u_m associated with MO coupling is given by $u_m = (1/4)\mathrm{Re}\mathcal{U}_m$, where

$$\mathcal{U}_m = \begin{pmatrix} E_{S+}^* & E_{S-}^* \end{pmatrix} \epsilon_m \begin{pmatrix} E_{I+} \\ E_{I-} \end{pmatrix}, \quad (1)$$

and where $\epsilon_m = \epsilon_{m0} + \epsilon_{m+} m_{+'} + \epsilon_{m-} m_{-'}$ is a transverse permittivity tensor. The static part ϵ_{m0} is given by Eq. (A2) of Appendix A. The diagonal elements of ϵ_{m0} give rise to the static Faraday effect, whereas the static Voigt (Cotton–Mouton) effect originates from the off-diagonal elements of ϵ_{m0} [see Eq. (A2)]. The terms $\epsilon_{m+} m_{+'}$ and $\epsilon_{m-} m_{-'}$ account for the effect of magnetization precession, where $\epsilon_{m\pm}$ is given by Eq. (A3) of Appendix A, and $m_{\pm'}$ represent amplitudes of magnetization precession. Note that the matrix $\epsilon_{m\pm}$ is proportional to $e^{\pm i\varphi}$, where φ is the azimuthal angle

[see Eq. (A3)]. The spherical symmetry of the FSR is partially broken by the two CFs that are employed for holding it (see Fig. 1).

In the semiclassical approximation, V_{SB} is derived from $u_m = (1/4)\mathrm{Re}\mathcal{U}_m$ [see Eq. (1)]. Consider a pair of optical modes having normalized scalar spatial waveforms, which in spherical coordinates are expressed as $u_{n'}(r, \theta, \varphi)$ and $u_{n''}(r, \theta, \varphi)$, respectively. The contribution of this pair to the total interaction term V_{SB}, which is denoted by $V_{n',n''}$, is expressed as

$$V_{n',n''} = a^{\dagger}_{n'} a_{n''} \left(g_{n',n'',+} b^{\dagger} + g_{n',n'',-} b \right) + \text{h.c.}, \tag{2}$$

where a_n (b) is an annihilation operator for the nth optical mode (magnon mode), and h.c. stands for Hermitian conjugate. The coupling coefficients $g_{n',n'',\pm}$ are given by (recall that in our experiment the static magnetic field is normal to the light propagation direction)

$$\hbar^{-1} g_{n',n'',\pm} \simeq g_0 \int \mathrm{d}\mathbf{r}'\, e^{\pm i\varphi} u_{n'}(\mathbf{r}') u^{*}_{n''}(\mathbf{r}'), \tag{3}$$

where $g_0 = \omega_L Q_s / \left(8 n_0^2 N_s^{1/2}\right)$ and N_s is the number of FSR spins ($N_s = 3.4 \times 10^{16}$ for the FSR under study). For YIG in the telecom band (free space wavelength $\lambda_0 \simeq 1550$ nm), the refractive index is $n_0 = 2.19$, and the dimensionless MO coupling coefficient is $Q_s \simeq 10^{-4}$,[33] and thus $g_0/(2\pi) = 2.7$ Hz. The overlap integral in Eq. (3) represents a photon-magnon scattering selection rule.[11,12]

The ratio of sideband output optical power to the input optical power is denoted by η_{SB}. The largest value of η_{SB} is obtained at the triple resonance,[11] for which the MW driving is tuned to the FSR resonance ω_m, the laser frequency ω_L matches the frequency of one optical mode, and the second one has a frequency detuned from ω_L by ω_m. For this case $\eta_{SB} \simeq (2 n_0 R_s g_0/c)^2 N_m$ [it is assumed that the overlap integral in Eq. (3) is of order unity], where N_m is the averaged number of excited magnons in steady state. For the case where the MWA is nearly critically coupled to the FSR, at resonance $N_m \simeq P_p/(\hbar \omega_m \kappa_m)$, where κ_m is the FSR damping rate. The values of $P_p = 20$ dBm, $\omega_m/(2\pi) = 3.8$ GHz and $\kappa_m/(2\pi) = 1$ MHz yield $\eta_{SB} \simeq 10^{-5}$. This rough estimate agrees with the experimentally observed value of η_{SB} (see Fig. 5).

V. KERR NONLINEARITY

Magnetic anisotropy gives rise to Kerr nonlinearity in the FSR response.[34] The nonlinearity can be exploited for modulation amplification.[35] The anisotropy-induced Kerr coefficient K_M is given by $K_M = \hbar \gamma_e^2 K_{c1} / \left(V_s M_s^2\right)$, where K_{c1} is the first-order anisotropy constant, $V_s = 4\pi R_s^3/3$ is the FSR volume, and M_s is the saturation magnetization.[34] For YIG $K_{c1} = -610\,\mathrm{J/m^3}$ at 297 K, and $M_s = 140$ kA/m, hence for $R_s = 125\,\mu$m the expected value of the Kerr coefficient is given by $K_M/(2\pi) = -2.0 \times 10^{-9}$ Hz. The Kerr nonlinearity is expected to give rise to bistability in the FSR response to externally applied driving.

Modulation measurements in the nonlinear regime are shown in Fig. 6. The results indicate that the Kerr coefficient K_M is negative (giving rise to softening). For the plots shown in the top (bottom) row of Fig. 6, the microwave driving frequency is swept upwards (downwards). The dependency on sweeping direction is attributed to nonlinearity-induced bistability, which, in turn, gives rise to hysteresis.

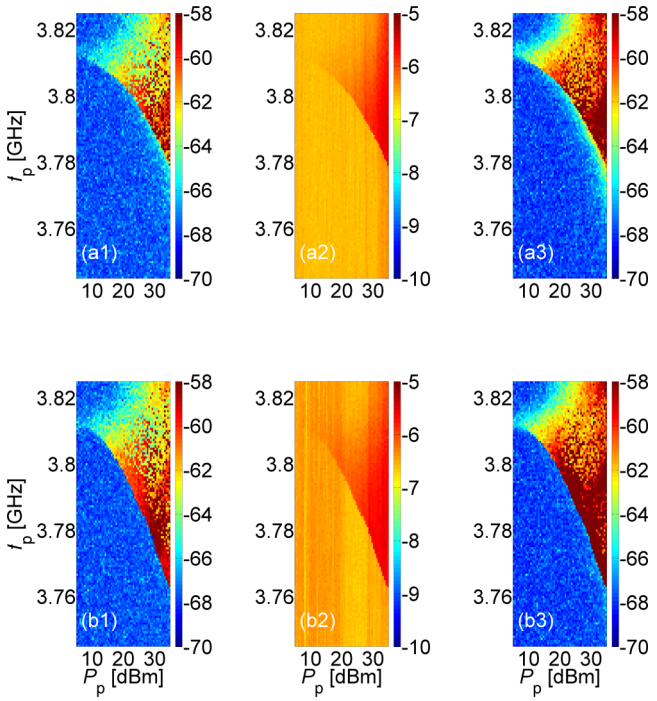

FIG. 6. Spectral peaks (in dBm units) in the nonlinear regime as a function of MW driving power P_p. The intensity of the left (right) sideband at wavelength $\lambda_L - \lambda_{SB}$ ($\lambda_L + \lambda_{SB}$) is shown in the plots in the left (right) column, whereas the plots in the central column show the intensity of the central optical peak (at TL1 wavelength λ_L). For the plots shown in the top (bottom) row, the frequency f_p is swept upwards (downwards).

VI. SUMMARY

In summary, polarization-selective SSM in the telecom band is achieved using an FSR strongly coupled to an LGR. The modulator can be used in a wide optical band, and it is compatible with ultra low temperatures. Future study will explore potential applications, including quantum state readout of superconducting circuits.

ACKNOWLEDGMENTS

This work was supported by the Israeli Science Foundation, the Israeli Ministry of Science, and the Technion Security Research Foundation.

AUTHOR DECLARATIONS

Conflict of Interest

The authors have no conflicts to disclose.

Author Contributions

Banoj Kumar Nayak: Data curation (lead); Investigation (lead); Writing – original draft (equal). **Eyal Buks:** Formal analysis (lead); Supervision (lead); Writing – original draft (equal).

DATA AVAILABILITY

The data that support the findings of this study are available from the corresponding author upon reasonable request.

APPENDIX A: TRANSVERSE PERMITTIVITY TENSOR

The evolution of electromagnetic waves propagating inside a magnetized medium is governed by a 3×3 permittivity tensor.[36–38] Consider a Cartesian coordinate system (x, y, z), for which the propagation direction is parallel to the z direction. In this system, the static magnetic field (magnetization vector) is parallel to a unit vector denoted by $\hat{\boldsymbol{h}}$ ($\hat{\boldsymbol{m}}$). The angle between $\hat{\boldsymbol{h}} = (h_x, h_y, h_z) = (\sin\theta\cos\varphi, \sin\theta\sin\varphi, \cos\theta)$ and $\hat{\boldsymbol{m}} = (m_x, m_y, m_z)$ is assumed to be small.

From the 3×3 permittivity tensor, a 2×2 transverse permittivity tensor $\boldsymbol{\epsilon}_{\mathrm{T}}$ can be derived. In a basis of circular SOP, $\boldsymbol{\epsilon}_{\mathrm{T}}$ is given by $\boldsymbol{\epsilon}_{\mathrm{T}} = n_0^2 I + \boldsymbol{\epsilon}_{\mathrm{m}}$, where n_0 is the medium refractive index, I is the 2×2 identity matrix, and the 2×2 matrix $\boldsymbol{\epsilon}_{\mathrm{m}}$ (in a basis of circular SOPs) is given by[39]

$$\frac{\boldsymbol{\epsilon}_{\mathrm{m}}}{n_0^2} = \begin{pmatrix} Q_{\mathrm{s}} m_z & Q_{\mathrm{s}}^2 m_-^2 \\ Q_{\mathrm{s}}^2 m_+^2 & -Q_{\mathrm{s}} m_z \end{pmatrix}, \tag{A1}$$

where $m_\pm = (m_x \pm i m_y)/\sqrt{2}$. For YIG in the telecom band, the refractive index is $n_0 = 2.19$, and the dimensionless MO coupling coefficient is $Q_{\mathrm{s}} \simeq 10^{-4}$.[33]

The eigenvalues of $\boldsymbol{\epsilon}_{\mathrm{m}}/n_0^2$ (A1) are given by $\pm Q_{\mathrm{s}}\sqrt{m_z^2 + Q_{\mathrm{s}}^2 m_-^2 m_+^2}$. For the Faraday configuration, for which $m_x = m_y = 0$ and $m_z = 1$, i.e., $\hat{\boldsymbol{m}}$ is parallel to the propagation direction, the eigenvectors of $\boldsymbol{\epsilon}_{\mathrm{m}}/n_0^2$ represent circular SOPs, the corresponding eigenvalues are $\pm Q_{\mathrm{s}}$, and MO coupling gives rise to circular birefringence, whereas for the Voigt (Cotton–Mouton) configuration, for which $m_z = 0$ and $m_x^2 + m_y^2 = 1$, i.e., $\hat{\boldsymbol{m}}$ is perpendicular to the propagation direction, the eigenvectors of $\boldsymbol{\epsilon}_{\mathrm{m}}/n_0^2$ represent colinear SOPs, the corresponding eigenvalues are $\pm Q_{\mathrm{s}}^2/2$ [note that $m_-^2 m_+^2 = \left(m_x^2 + m_y^2\right)^2/4$], and MO coupling gives rise to colinear birefringence. Note that for the Faraday configuration, the SOP rotation angle that is accumulated over a traveling distance of a single optical wavelength is $2\pi Q_{\mathrm{s}}$.

To describe the effect of magnetization precession on $\boldsymbol{\epsilon}_{\mathrm{m}}$, it is convenient to express $\hat{\boldsymbol{m}}$ (magnetization unit vector) as a sum of parallel and perpendicular components, with respect to $\hat{\boldsymbol{h}}$ (magnetic field unit vector). In a Cartesian coordinate system (x', y', z'), for which the static magnetic field is parallel to the z' direction, the unit vector parallel to the magnetization vector is expressed as $\hat{\boldsymbol{m}}' = m_{x'}\hat{\boldsymbol{x}}' + m_{y'}\hat{\boldsymbol{y}}' + m_{z'}\hat{\boldsymbol{z}}' = m_{+'}\hat{\boldsymbol{u}}'_+ + m_{-'}\hat{\boldsymbol{u}}'_- + m_{z'}\hat{\boldsymbol{z}}'$, where $\hat{\boldsymbol{u}}'_\pm = (\hat{\boldsymbol{x}}' \pm i\hat{\boldsymbol{y}}')/\sqrt{2}$, and where $m_{\pm'} = (m_{x'} \mp i m_{y'})/\sqrt{2}$. The unit vectors $\hat{\boldsymbol{m}}$ and $\hat{\boldsymbol{m}}'$ are related by $\hat{\boldsymbol{m}} = R_{\hat{\boldsymbol{h}}}^{-1}\hat{\boldsymbol{m}}'$, where for a given unit vector $\hat{\boldsymbol{n}}$, the rotation matrix $R_{\hat{\boldsymbol{n}}}$ is defined by the relation $R_{\hat{\boldsymbol{n}}}\hat{\boldsymbol{n}} = \hat{\boldsymbol{z}}$ and, thus, $\hat{\boldsymbol{m}} = m_{+'}\hat{\boldsymbol{v}}_+ + m_{-'}\hat{\boldsymbol{v}}_- + m_{z'}R_{\hat{\boldsymbol{h}}}^{-1}\hat{\boldsymbol{z}}'$, where $\hat{\boldsymbol{v}}_\pm = R_{\hat{\boldsymbol{h}}}^{-1}\hat{\boldsymbol{u}}'_\pm$. The matrix elements of the 3×3 rotation matrix $R_{\hat{\boldsymbol{h}}}$ are given by $R_{11} = 1 + (\cos\theta - 1)\cos^2\varphi$, $R_{22} = 1 + (\cos\theta - 1)\sin^2\varphi$, $R_{12} = R_{21} = (1/2)(\cos\theta - 1)\sin(2\varphi)$, $R_{31} = -R_{13} = \sin\theta\cos\varphi$, $R_{32} = -R_{23} = \sin\theta\sin\varphi$, and $R_{33} = \cos\theta$. The following holds $\hat{\boldsymbol{v}}_\pm = \cos^2(\theta/2)\hat{\boldsymbol{u}}_\pm - e^{\pm 2i\varphi}\sin^2(\theta/2)\hat{\boldsymbol{u}}_\mp - 2^{-1/2}e^{\pm i\varphi}(\sin\theta)\hat{\boldsymbol{z}}$, hence $\hat{\boldsymbol{m}} = \mu_+\hat{\boldsymbol{u}}_+ + \mu_-\hat{\boldsymbol{u}}_- + \mu_z\hat{\boldsymbol{z}} + m_{z'}\hat{\boldsymbol{h}}$, where $\mu_\pm = m_{\pm'}\cos^2(\theta/2) - m_{\mp'}e^{\mp 2i\varphi}\sin^2(\theta/2)$ and $\mu_z = -2^{-1/2}(m_{+'}e^{i\varphi} + m_{-'}e^{-i\varphi})\sin\theta$ and, thus, $m_\pm = \mu_\mp + 2^{-1/2}m_{z'}e^{\mp i\varphi}\sin\theta$.

The assumption that the angle between the static magnetic field and the magnetization vector is small implies that $m_{z'} \simeq 1$ and $|m_{\pm'}| \ll 1$. To first order in $|m_{\pm'}|$, $\boldsymbol{\epsilon}_{\mathrm{m}}$ can be expanded as $\boldsymbol{\epsilon}_{\mathrm{m}} = \boldsymbol{\epsilon}_{\mathrm{m}0} + \boldsymbol{\epsilon}_{\mathrm{m}+}m_{+'} + \boldsymbol{\epsilon}_{\mathrm{m}-}m_{-'}$, where $\boldsymbol{\epsilon}_{\mathrm{m}0}$, which is given by [compare with Eq. (A1)]

$$\frac{\boldsymbol{\epsilon}_{\mathrm{m}0}}{n_0^2} = \begin{pmatrix} Q_{\mathrm{s}}\cos\theta & \frac{Q_{\mathrm{s}}^2 e^{2i\varphi}\sin^2\theta}{2} \\ \frac{Q_{\mathrm{s}}^2 e^{-2i\varphi}\sin^2\theta}{2} & -Q_{\mathrm{s}}\cos\theta \end{pmatrix}, \tag{A2}$$

accounts for static magnetization, and where $\boldsymbol{\epsilon}_{\mathrm{m}\pm}$, which is given by

$$\frac{\boldsymbol{\epsilon}_{\mathrm{m}\pm}}{n_0^2} = \frac{Q_{\mathrm{s}}e^{\pm i\varphi}\sin\theta}{\sqrt{2}} \begin{pmatrix} -1 & \pm Q_{\mathrm{s}}(1 \pm \cos\theta) \\ \mp Q_{\mathrm{s}}(1 \mp \cos\theta) & 1 \end{pmatrix}, \tag{A3}$$

accounts for magnetization precession.

REFERENCES

[1] V. Lazzarini, J. Timoney, and T. Lysaght, "Asymmetric-spectra methods for adaptive FM synthesis" (2008).
[2] W. Li, W. T. Wang, L. X. Wang, and N. H. Zhu, "Optical vector network analyzer based on single-sideband modulation and segmental measurement," IEEE Photonics J. **6**(2), 1–8 (2014).
[3] S. Shimotsu, S. Oikawa, T. Saitou, N. Mitsugi, K. Kubodera, T. Kawanishi, and M. Izutsu, "Single side-band modulation performance of a $LiNbO_3$ integrated modulator consisting of four-phase modulator waveguides," IEEE Photonics Technol. Lett. **13**(4), 364–366 (2001).
[4] B. Z. Rameshti, S. V. Kusminskiy, J. A. Haigh, K. Usami, D. Lachance-Quirion, Y. Nakamura, C.-M. Hu, H. X. Tang, G. E. W. Bauer, and Y. M. Blanter, "Cavity magnonics," Phys. Rep. **979**, 1–61 (2022).
[5] S. V. Kusminskiy, "Cavity optomagnonics," in *Optomagnonic Structures: Novel Architectures for Simultaneous Control of Light and Spin Waves* (World Scientific, 2021), pp. 299–353.
[6] N. Zhu, X. Zhang, X. Han, C.-L. Zou, and H. X. Tang, Phys. Rev. Appl. **18**(2), 024046 (2022).
[7] D. M. Juraschek, D. S. Wang, and P. Narang, "Sum-frequency excitation of coherent magnons," Phys. Rev. B **103**(9), 094407 (2021).
[8] V. A. S. V. Bittencourt, I. Liberal, and S. V. Kusminskiy, "Light propagation and magnon-photon coupling in optically dispersive magnetic media," Phys. Rev. B **105**(1), 014409 (2022).
[9] X. Zhang, N. Zhu, C.-L. Zou, and H. X. Tang, "Optomagnonic whispering gallery microresonators," Phys. Rev. Lett. **117**(12), 123605 (2016).
[10] D. D. Stancil and A. Prabhakar, *Spin Waves* (Springer, 2009).
[11] J. A. Haigh, A. Nunnenkamp, A. J. Ramsay, and A. J. Ferguson, "Triple-resonant Brillouin light scattering in magneto-optical cavities," Phys. Rev. Lett. **117**(13), 133602 (2016).

[12]A. Osada, A. Gloppe, Y. Nakamura, and K. Usami, "Orbital angular momentum conservation in Brillouin light scattering within a ferromagnetic sphere," New J. Phys. **20**(10), 103018 (2018).
[13]A. Osada, R. Hisatomi, A. Noguchi, Y. Tabuchi, R. Yamazaki, K. Usami, M. Sadgrove, R. Yalla, M. Nomura, and Y. Nakamura, "Cavity optomagnonics with spin-orbit coupled photons," Phys. Rev. Lett. **116**(22), 223601 (2016).
[14]S. Sharma, Y. M. Blanter, and G. E. W. Bauer, "Light scattering by magnons in whispering gallery mode cavities," Phys. Rev. B **96**(9), 094412 (2017).
[15]E. Almpanis, "Dielectric magnetic microparticles as photomagnonic cavities: Enhancing the modulation of near-infrared light by spin waves," Phys. Rev. B **97**(18), 184406 (2018).
[16]R. Zivieri, P. Vavassori, L. Giovannini, F. Nizzoli, E. E. Fullerton, M. Grimsditch, and V. Metlushko, "Stokes–anti-stokes Brillouin intensity asymmetry of spin-wave modes in ferromagnetic films and multilayers," Phys. Rev. B **65**(16), 165406 (2002).
[17]B. Desormiere and H. Le Gall, "Interaction studies of a laser light with spin waves and magnetoelastic waves propagating in a YIG bar," IEEE Trans. Magn. **8**(3), 379–381 (1972).
[18]Z.-X. Liu, B. Wang, H. Xiong, and Y. Wu, "Magnon-induced high-order sideband generation," Opt. Lett. **43**(15), 3698–3701 (2018).
[19]C.-Z. Chai, Z. Shen, Y.-L. Zhang, H.-Q. Zhao, G.-C. Guo, C.-L. Zou, and C.-H. Dong, "Single-sideband microwave-to-optical conversion in high-Q ferrimagnetic microspheres," Photonics Res. **10**(3), 820–827 (2022).
[20]N. Zhu, X. Zhang, X. Han, C.-L. Zou, C. Zhong, C.-H. Wang, L. Jiang, and H. X. Tang, "Waveguide cavity optomagnonics for microwave-to-optics conversion," Optica **7**(10), 1291–1297 (2020).
[21]J. Li, Y.-P. Wang, W.-J. Wu, S.-Y. Zhu, and J. You, "Quantum network with magnonic and mechanical nodes," PRX Quantum **2**(4), 040344 (2021).
[22]W. Wettling, M. G. Cottam, and J. R. Sandercock, "The relation between one-magnon light scattering and the complex magneto-optic effects in YIG," J. Phys. C: Solid State Phys. **8**(2), 211 (1975).
[23]M. G. Cottam and D. J. Lockwood, *Light Scattering in Magnetic Solids* (Wiley, New York, 1986).
[24]T. Liu, X. Zhang, H. X. Tang, and M. E. Flatté, "Optomagnonics in magnetic solids," Phys. Rev. B **94**(6), 060405 (2016).
[25]J. A. Haigh, A. Nunnenkamp, and A. J. Ramsay, "Polarization dependent scattering in cavity optomagnonics," Phys. Rev. Lett. **127**(14), 143601 (2021).
[26]R. Hisatomi, A. Noguchi, R. Yamazaki, Y. Nakata, A. Gloppe, Y. Nakamura, and K. Usami, "Helicity-changing Brillouin light scattering by magnons in a ferromagnetic crystal," Phys. Rev. Lett. **123**(20), 207401 (2019).
[27]R. Hisatomi, A. Osada, Y. Tabuchi, T. Ishikawa, A. Noguchi, R. Yamazaki, K. Usami, and Y. Nakamura, "Bidirectional conversion between microwave and light via ferromagnetic magnons," Phys. Rev. B **93**(17), 174427 (2016).
[28]D. M. Baney, B. Szafraniec, and A. Motamedi, "Coherent optical spectrum analyzer," IEEE Photonics Technol. Lett. **14**(3), 355–357 (2002).
[29]M. Goryachev, W. G. Farr, D. L. Creedon, Y. Fan, M. Kostylev, and M. E. Tobar, "High-cooperativity cavity QED with magnons at microwave frequencies," Phys. Rev. Appl. **2**(5), 054002 (2014).
[30]D. Zhang, W. Song, and G. Chai, "Spin-wave magnon-polaritons in a split-ring resonator/single-crystalline YIG system," J. Phys. D: Appl. Phys. **50**(20), 205003 (2017).
[31]C. Mathai, O. Shtempluck, and E. Buks, "Thermal instability in a ferrimagnetic resonator strongly coupled to a loop-gap microwave cavity," Phys. Rev. B **104**, 054428 (2021).
[32]B. K. Nayak, C. Mathai, D. Meirom, O. Shtempluck, and E. Buks, "Optical interface for a hybrid magnon–photon resonator," Appl. Phys. Lett. **120**(6), 062404 (2022).
[33]D. L. Wood and J. P. Remeika, "Effect of impurities on the optical properties of yttrium iron garnet," J. Appl. Phys. **38**(3), 1038–1045 (1967).
[34]Y.-P. Wang, G.-Q. Zhang, D. Zhang, X.-Q. Luo, W. Xiong, S.-P. Wang, T.-F. Li, C.-M. Hu, and J. Q. You, "Magnon Kerr effect in a strongly coupled cavity-magnon system," Phys. Rev. B **94**(22), 224410 (2016).
[35]C. Mathai, S. Masis, O. Shtempluck, S. Hacohen-Gourgy, and E. Buks, "Frequency mixing in a ferrimagnetic sphere resonator," Euro. Phys. Lett. **131**, 67001 (2020).
[36]M. L. Freiser, "A survey of magnetooptic effects," IEEE Trans. Magn. **4**(2), 152–161 (1968).
[37]A. D. Boardman and M. Xie, "Magneto-optics: A critical review," in *Introduction to Complex Mediums for Optics and Electromagnetics* (SPIE, 2003), Vol. 123, p. 197.
[38]A. D. Boardman and L. Velasco, "Gyroelectric cubic-quintic dissipative solitons," IEEE J. Sel. Top. Quantum Electron. **12**(3), 388–397 (2006).
[39]E. Buks and B. K. Nayak, "Quantum measurement with recycled photons," Phys. Rev. B **105**(1), 014421 (2022).